Icarus **145**, 108–121 (2000)
doi:10.1006/icar.1999.6323, available online at http://www.idealibrary.com on IDEAL®

Interpreting the Elliptical Crater Populations on Mars, Venus, and the Moon

William F. Bottke, Jr.

Center for Radiophysics and Space Research, Cornell University, Ithaca, New York 14853-6801
E-mail: bottke@astrosun.tn.cornell.edu

Stanley G. Love

Johnson Space Center, Mail Code CB, 2101 NASA Road 1, Houston, Texas 77058

David Tytell

Division of Geological and Planetary Sciences, California Institute of Technology, M/S 170-25, Pasadena, California 91125

and

Timothy Glotch

Center for Radiophysics and Space Research, Cornell University, Ithaca, New York 14853-6801

Received July 17, 1998; revised December 2, 1999

Asteroids or comets striking a planetary surface at very shallow angles produce elliptical-shaped craters. According to laboratory impact experiments (D. E. Gault and J. A. Wedekind 1978, *Proc. Lunar Planet. Sci. Conf. 9th***, 3843–3875), elliptical craters result from impact angles within $\sim 5^\circ$ of horizontal and less than 1% of projectiles with isotropic impact trajectories create elliptical craters. This result disagrees with survey results which suggest that approximately 5% of all kilometer-sized craters formed on Mars, Venus, and the Moon have elliptical shapes.**

To explain this discrepancy, we examined the threshold incidence angle necessary to produce elliptical craters in laboratory impact experiments. Recent experiments show that aluminum targets produce elongated craters at much steeper impact angles than sand targets. This suggests that target properties are as important as the projectile's impact angle in determining the eventual ellipticity of the crater. Creating a model which interpolates between impact data produced using sand and aluminum targets, we derive a new elliptical crater threshold angle of 12° from horizontal for Mars, Venus, and the Moon. This leads to a predicted proportion of elliptical craters that matches observations within uncertainty given a random projectile population. We conclude that the observed proportion of elliptical craters on these bodies is a natural by-product of projectiles striking at random angles, and that no additional formation mechanisms are needed.

Key Words: **impact processes; Mars, surface; Moon, surface; Venus, surface.**

1. INTRODUCTION

Asteroids or comets striking planetary surfaces generally produce circular impact craters, even when those objects hit at angles substantially off vertical (Melosh 1989). Elliptical impact craters are produced when impact angles are low relative to the horizontal. These results have been verified by laboratory experiments consisting of small aluminum and pyrex spheres shot at several km/s into sand or aluminum targets (Gault and Wedekind 1978, hereafter GW78; Christiansen *et al.* 1993, hereafter C93; Burchell and Mackay 1998). GW78 found that projectiles shot at angles 4.75° from the horizontal or lower into sand targets produce craters which are at least 1.1 times as long as they are wide. We refer to these values as a crater's "ellipticity" (ε), defined as the quotient of its maximum and minimum rim-to-rim diameters. Incidence angles $>4.75^\circ$ produce less elongated craters, with the transition between circular and elongated craters occurring somewhere near 10°.

C93 found that projectiles shot into aluminum at angles $<25^\circ$ from the horizontal produce elliptical craters. This higher threshold angle suggests that target (and projectile) material properties can affect crater ellipticity, often in complex ways (Burchell and Mackey 1998). Since sand is considered a better analog to terrestrial planet surfaces than metal for understanding gravity-controlled excavation from an impact site (e.g., Melosh 1989), GW78's results alone have been used to understand elliptical

0019-1035/00 $35.00

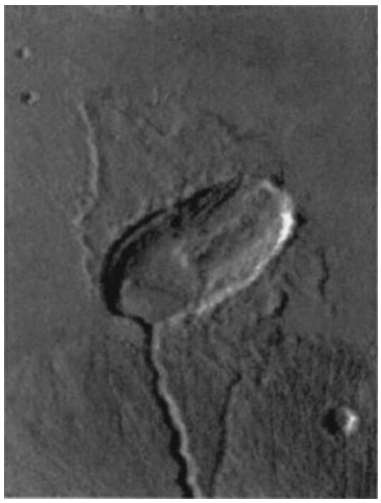

FIG. 1. Martian crater formed by oblique impact. The crater is located at 25° latitude, 97.5° longitude. It is 35 × 18 km in diameter, giving it an ellipticity $\varepsilon = 1.9$. Note the crater's central ridge and well defined butterfly-wing ejecta pattern above the crater. The part of the ejecta blanket below the crater has been covered by a volcano and a lava channel. This crater is SL82, No. 37.

crater formation. Thus, the accepted threshold angle for elliptical crater formation ($\varepsilon \geq 1.1$) has been $<4.75°$. An example of such a crater can be found in Fig. 1; comparable elliptical craters have been observed on all of the terrestrial planets.

The crater in Fig. 1 also has an ejecta blanket shaped like a "butterfly-wing." GW78's laboratory experiments suggest these ejecta blankets are produced at impact angles $<10°$, with the wings perpendicular to the symmetry axis lying along the impact trajectory. Since this threshold angle is higher than the angle needed for forming an elliptical crater, some nearly circular craters will have butterfly-wing ejecta blankets as well.

Survey results show that elliptical craters on Mars are much more likely to have butterfly-wing ejecta patterns than elliptical craters on the Moon and Mercury. On the Moon, the crater Messier (14 × 6 km) is the only elliptical crater its size or larger with a distinctive butterfly-shaped ejecta blanket (Schultz and Lutz-Garihan 1982) on the lunar maria. The preponderance of butterfly ejecta patterns on Mars is difficult to interpret. One possibility is that Mars had more low-angle impactors striking its surface than other planets. Another possibility is that the martian surface or atmosphere has some property which helps produce (or preserve) butterfly-shaped ejecta blankets.

To better understand this issue, Schultz and Lutz-Garihan (1982, hereafter SL82) examined martian craters larger than 5 km for high ellipticity values, butterfly-wing ejecta patterns, and other signs of oblique impactors. They found several martian surfaces with high fractions of elliptical craters: Lunae Planum ($5 \pm 0.4\%$), Syrtis Major Planitia ($3 \pm 0.5\%$), and the cratered plains near Uranius Tholus ($8 \pm 0.4\%$). Overall, SL82 estimated that ~5% of Mars's large craters had substantial elongation and/or butterfly-shaped ejecta blankets.

SL82 noted this outcome is hard to reconcile with GW78's threshold angle for elliptical crater formation ($\leq 4.75°$ to get $\varepsilon \geq 1.1$). Since the probability of randomly flying particles impacting a planet at $\leq\theta$ (an angle measured from the horizontal) is $\sin^2\theta$ (Shoemaker 1962), the fraction of projectiles striking Mars at $\theta \leq 4.75°$ should only be 0.7%. Thus, the observed fraction of martian elliptical craters (~5%) is much larger than predicted.

There are several possible ways of explaining this apparent excess. (i) There are fewer elliptical craters on Mars than suggested by SL82. (ii) The laboratory experiments used to determine the threshold angle needed to produce elliptical craters are not applicable to kilometer-sized projectiles. (iii) The excess is real and the impact population had anisotropic impact angles. SL82 suggested that if (iii) were correct, the elongated crater population on Mars might have been enhanced by an ancient population of moonlets which spiraled inward under the influence of tidal forces and atmospheric drag to strike the planet at shallow angles.

In this paper, we will examine each of these potential solutions. For (i), we reexamined the portion of the SL82's elliptical crater set found within ~48° of the equator and compared it to an independent survey (Barlow 1988) and to two new crater surveys performed on the Moon and Venus. (Section 2). For (ii), we used results of laboratory impact experiments to reformulate the threshold impact angle for producing markedly elliptical craters (Section 3). For (iii), we numerically modeled SL82's "spiraling moonlet" scenario, since it provides the best alternative explanation for an excess of elliptical martian craters (Section 4). Finally, we summarize our conclusions (Section 5).

2. THE ELLIPTICAL CRATER POPULATION ON MARS, VENUS, AND THE MOON

Here we examine the fractions of elliptical craters on several terrestrial planets. Similar fractions would imply that impactor populations probably had isotropic impact angles and that elliptical crater formation processes are similar across the terrestrial planets. The abundance of butterfly-shaped ejecta blankets on Mars might then be explained as some interaction between Mars's surface or atmosphere during crater formation. Dissimilar fractions of elliptical craters would imply that impact angles were anisotropic for some impacting populations, or that crater formation processes are a stronger function of planetary surface properties than previously believed. Either reason would provide a natural explanation for why Mars has a large fraction of butterfly-wing ejecta blankets surrounding its craters.

2.1. Reexamining Mars's Elongated Crater Population

In order to check the elliptical crater survey of SL82, we reexamined their listed craters using the criteria listed in their text. Specifically, they sought craters with characteristics similar to those formed in oblique angle laboratory impacts ($\leq 5°$;

$\varepsilon \geq 1.1$) or observed in the lunar crater Messier. Diagnostic features included crater ellipticity and some combination of the following features: butterfly-wing ejecta blankets, saddle-shaped rims, and median floor ridges. We refer to these crater types here as "elliptical-plus" craters. Elliptical craters having less than two of these features were supposed to be excluded from SL82's survey. To eliminate potential secondary craters, SL82 excluded craters smaller than 3 km near recent major impacts and those with characteristic herringbone patterns. Doublet, multiple, or irregular craters in the same region which lacked the butterfly ejecta pattern were also excluded.

Overall, SL82 identified 176 elliptical-plus craters with minor axis diameters larger than 3 km between latitudes $\pm 65^\circ$. Most were found lying between $\pm 50^\circ$, far from polar regions where erosion rates can more readily erase ejecta blankets and other features. The locations of these craters were presented in SL82's Appendix A. A reinvestigation of these craters for this paper, however, indicates that several craters were placed in the wrong category. For example, several circular craters with butterfly-wing ejecta blankets were listed in Appendix A. According to SL82's selection criteria, these craters should have been excluded.

As a consistency check, we examined an independent crater survey. Barlow (1988, hereafter B88) has surveyed the martian crater population and recorded crater ellipticity. She identified 212 craters larger than 2 km with $\varepsilon \geq 1.2$ between latitudes $\pm 75^\circ$. Most of these craters are larger than SL82's 3-km cutoff diameter. (Note: To be conservative, we chose $\varepsilon \geq 1.2$ as our cutoff rather than SL82's $\varepsilon \geq 1.1$, since many of B88's craters are eroded enough that they lack the diagnostic features of SL82's elliptical-plus craters).

To examine the craters, we used the on-line Mars Multi-Scale Map website (C. J. Hamilton, pers. commun. 1998), which contains Viking images between latitudes of $\pm 47.5^\circ$. This area included about 90% of SL82's listed craters, acceptable for our purposes. Craters from either survey that were outside this region were excluded from this study. We found only 42 craters that were common to both SL82 and B88. These craters generally had large ellipticities and sharp features. Identifying the remaining craters was difficult and subjective since many were degraded or only marginally elongated.

We consider it plausible that some of SL82's 176 and B88's 212 elliptical craters were produced by postimpact modification effects. Potential mechanisms include: crater wall collapse, erosion, and faulting. To filter out such effects, and to account for possibly misclassified craters, we grouped SL82 and B88 craters into four subjective categories: "Likely," "Possible," "Unlikely," and "Omitted":

Likely. These craters have $\varepsilon \geq 1.1$ for SL82 craters or $\varepsilon \geq 1.2$ for B88 craters with (a) little to no apparent erosion, (b) possible central ridge, and (c) butterfly ejecta blanket. Characteristic (c) is not seen in every crater in this category. Figure 2 is an example (SL82 crater No. 107). Note its elliptical shape, the clear central ridge, and its ejecta "wings."

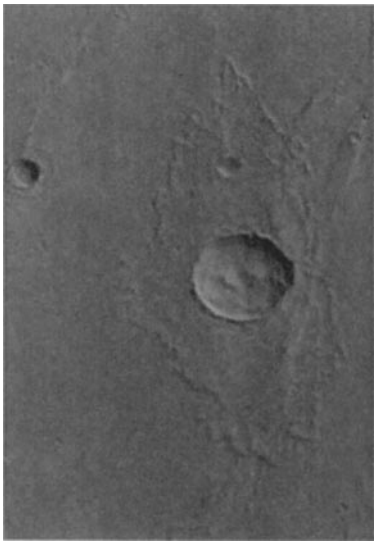

FIG. 2. "Likely" oblique impact crater located at -18° latitude, 72° longitude. Its dimensions are 18×15 km, yielding $\varepsilon = 1.1$. Note the strong butterfly-wing ejecta blanket just like that seen in Fig. 1. This crater is SL82, No. 107.

Possible. These craters have $\varepsilon \geq 1.1$ for SL82 craters or $\varepsilon \geq 1.2$ for B88 craters, with minor to medium levels of erosion, faulting, or crater wall collapse. We classified Fig. 3 (B88 crater No. 107) as a possible oblique impact. Though the feature is elongated, it has undergone significant alteration, which may or may not have affected its ellipticity.

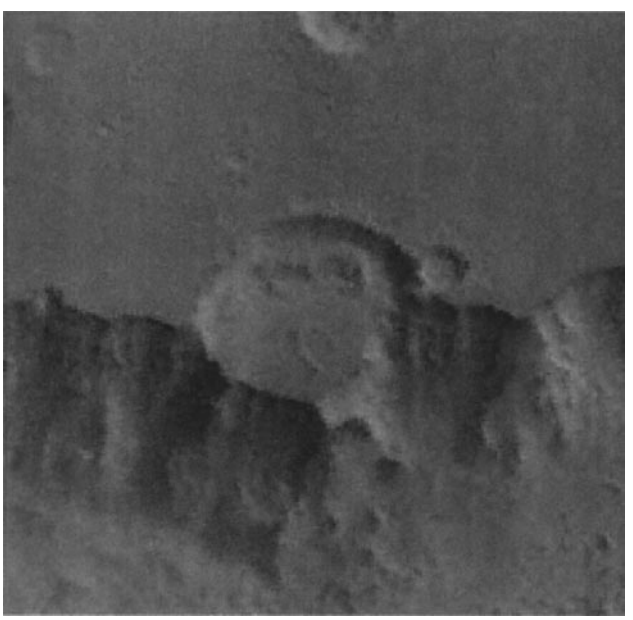

FIG. 3. "Possible" oblique impact crater located at -12° latitude, 48° longitude. Its dimensions are 17×13 km, yielding $\varepsilon = 1.4$. Since part of the crater is truncated by the canyon, we do not classify it as Likely. This crater is B88, No. 107.

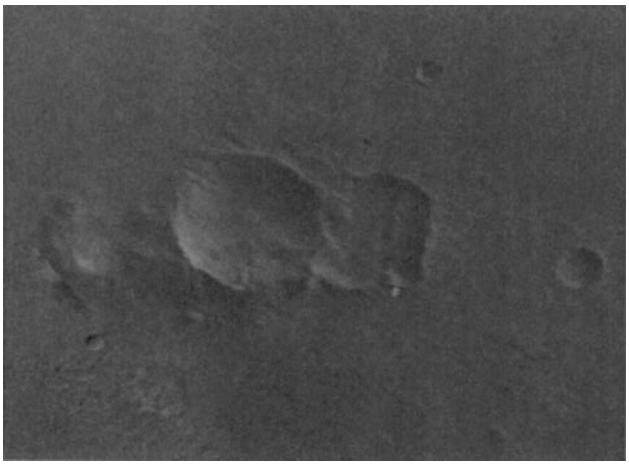

FIG. 4. "Unlikely" oblique impact crater located at -31° latitude, 272.5° longitude. Its dimensions are 13×5 km, yielding $\varepsilon = 2.6$. This feature is not an elliptical crater at all, but instead a doublet crater produced by two asteroids impacting Mars simultaneously. Note the shared crater wall. If the two craters had formed at different times, one crater's morphology would distinctly overlap the other. This crater is SL82, No. 163.

Unlikely. These craters have $\varepsilon < 1.1$ for SL82 craters or $\varepsilon < 1.2$ for B88 craters, with (a) high levels of suspected erosion, (b) another suspected formation mechanism (i.e., doublet craters, faulting), or (c) poor image quality. Erosion was the typical reason that craters were placed in this group. Fig. 4 (SL82 crater no. 163) is clearly not an elliptical crater. We interpret it to be a doublet crater formed by the impact of a binary asteroid (Bottke and Melosh 1996a,b). Comparable doublets have been found on all other terrestrial planets. We cannot rule out the possibility, however, that this doublet is attributable to an oblique impact with downrange decapitation of the impactor (Schultz and Gault 1990a).

Omitted. Craters were omitted when (a) their minimum diameter was smaller than 5 km; crater counts may only be complete to 5 km diameter (B88), (b) we were unable to find them at the referenced location, (c) they fell outside our latitude limitations, or (d) they were indistinguishable from surrounding circular craters in the field (i.e., the image in the Mars Multi-Scale Map was taken from an oblique angle, such that all of the craters in the field look elliptical). The last effect occurred most often at high latitudes.

The results of our survey and reanalysis is as follows. Out of a set of 346 craters (no overlaps), 102 were Likely, 121 were Possible, 28 were Unlikely, and 95 craters were Omitted (see Appendix A). Thus, 223 craters could be classified as Likely or Possible. Figure 5 shows the ellipticity of these craters plotted against their minimum diameter.

Calculating the global fraction of martian elliptical craters is impossible without first compensating for observational selection effects. Circular and elliptical craters have formed throughout martian history, but volcanism, tectonics, impacts, and erosion work to eliminate these features and to distort initially circular craters. This creates a dichotomy of hard-to-interpret cratered surfaces, with surveys biased toward detecting large old craters (which are too big to erase) and fresh young craters (which have not yet had time to be erased). For example, the dataset produced by B88 suggests that there are ~31,000 craters with diameters $\geq$5 km between latitudes $\pm$47.5, but that many of them are highly degraded. Thus, while B88's survey is complete, it cannot include the number of craters which have been obliterated over time.

To overcome these obstacles, SL82 counted diameter $D >$ 5 km craters on several ridged plains units (e.g., Lunae Planum, Syrtis Major Planitia) which are young and fresh. They then applied the derived fraction of elliptical-plus craters found there to the rest of Mars. SL82 found that Lunae Planum and Syrtis Major Planitia have $5 \pm 0.4\%$ and $3 \pm 0.5\%$ elliptical-plus craters, respectively. Unfortunately, no absolute crater counts in these regions were given, so we are unable to explicitly duplicate their work without an extensive survey of our own. We can, however, use our results to verify SL82's accuracy. B88's database indicates that the number of $D > 5$ km craters on Lunae Planum is 128, while the number on Syrtis Major Planitia is 207. Using our elliptical crater database (Appendix A), we find five Likely or Possible elliptical craters in each region. Since the total number of elliptical craters in each region did not change from SL82's estimates, we believe we would rederive SL82's estimated proportion of martian elliptical craters (~5%) if we had their crater counts and the exact sizes of the regions they surveyed. Using B88's $D > 5$ km data alone, we estimate that Lunae Planum and Syrtis Major Planitia have 3.9 and

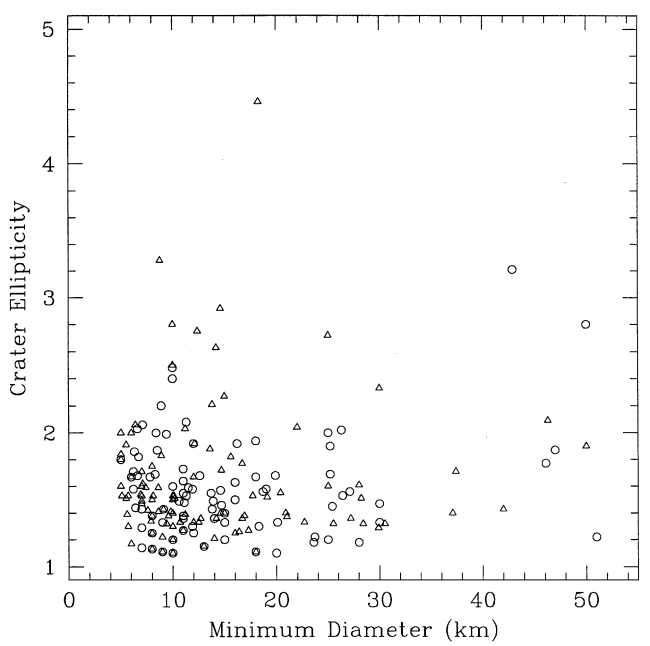

FIG. 5. Minimum crater diameter (km) plotted against ellipticity ε (ratio of maximum-to-minimum crater diameter) for 102 Likely craters (circles) and 121 Possible craters (triangles).

2.4% elliptical craters, respectively, in general agreement with SL82's results.

2.2. Survey of Elliptical Craters on the Lunar Mare

As far as we can know, elliptical (rather than elliptical plus) craters have not been surveyed on any terrestrial planet besides Mars. SL82 only describe a search for elliptical-plus craters. Unfortunately, without additional data, it is impossible to determine whether Mars's fraction of elliptical craters is typical or anomalous. To resolve this issue, we surveyed the sparsely cratered Lunar maria for elliptical craters using the selection criteria discussed above.

On the Maria, impact craters larger than a few kilometers tend to be distinct and relatively unmodified by other impact craters. We limited our survey to $\varepsilon \geq 1.2$ craters several kilometers in diameter or larger, mainly to avoid biasing our sample with secondaries. Craters in obvious rays, in nearby but nonmare terrain, and those which had been deformed by subsequent impacts or basaltic flooding were excluded.

Regions investigated included Mare Tranquillitatis, Mare Nectaris, Mare Vaporum, Mare Nubium, the east half of Mare Serenitatis, the west half of Mare Humorum, and parts of Oceanus Procellarum. For the last region, areas in the immediate vicinity of craters Copernicus and Kepler were excluded. More precisely, we studied Lunar Orbiter IV images 53, 54, 60, 61, 66, 72, 73, 77, 78, 85, 86, 90, 97, 113, 114, 120, 121, 126, 133, 138, 144, 149, 150, 156, 157, 162, and 169. Crater lengths and widths were measured using the NIH Image software package.

A total of 932 craters were measured, with the smallest being 2.3 km and the largest being 89 km (see Fig. 6). The surface was pristine enough that few craters were placed into the Unlikely category. Our results showed that 50 of the 932 craters (5.4%) were elliptical. This fraction does not change significantly with size; the subset of craters larger than 20 km in diameter has nearly the same percentage of elliptical craters. This indicates that our results have not been contaminated significantly by secondaries. The maximum ellipticity found among the 932 craters is 2.23. We found no butterfly-shaped ejecta blankets among our sample.

We conclude that even though the Moon is deficient in butterfly-shaped ejecta blankets relative to Mars, it has about the same fraction of elliptical craters as observed on Mars.

2.3. Survey of Elliptical Craters on Venus

We have also performed a preliminary survey of venusian elliptical craters. Venus's crater record is more difficult to interpret, since Venus's dense atmosphere causes some projectiles (especially small ones) to break up prior to impact. Factors such as the projectile's size, trajectory, velocity, composition, and internal structure determine whether the body can stay together long enough to form a "standard" crater or whether it disrupts and disperses, producing an irregular crater, a crater field, or no crater at all. Thus, we expected to see fewer big elongated craters than small ones, since big asteroids and comets are the least likely to suffer significant deformation in Venus's atmosphere. For our survey, we used crater images produced using Magellan's synthetic aperture radar. Coordinates and information on each Venusian craters can be found on-line at the U.S. Geological Survey (Schaber *et al.* 1998) and at the Lunar and Planetary Institute in Houston (R. Herrick, pers. commun. 1998).

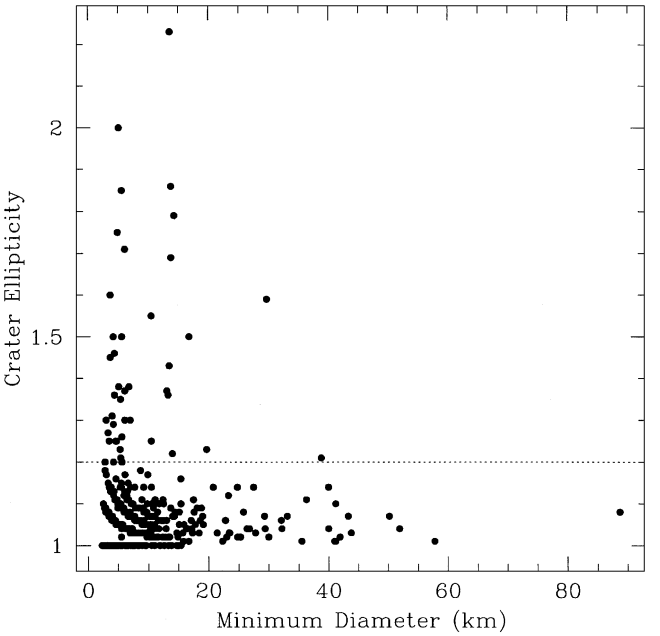

FIG. 6. Minimum crater diameter (km) plotted against ellipticity for 932 craters on the Lunar Maria. The smallest crater on the plot is 2.3 km. Note that to avoid observational selection effects, only the craters with ellipticities $\varepsilon \geq 1.2$ (dotted line) are considered elliptical.

Unfortunately for our purposes, Magellan CD images have been mapped using a sinusoidal projection, which keeps areas true but distorts features far from the central meridian. Remapping all the images using a Mercator projection, which distorts areas but keeps shapes more-or-less true, was deemed too labor-intensive for available student work time. To make the project more manageable, we broke our survey into two parts.

For the first part, we measured the elongation of 854 sinusoidally projected venusian craters, excluding those which were either highly degraded or clearly produced by multiple impacts. The smallest measured crater was 1.7 km, while the largest was 268.7 km. Our goal was to filter out most of the circular or nearly circular craters from the database; we consider it unlikely that many elongated craters distorted by a sinusoidal projection were turned into nearly circular craters. Our results showed that 185 of the 854 (22%) sinusoidally projected craters had major-to-minor axis ratios $\geq$1.2. This fraction drops to 14% (43 of 303) for craters with diameters $D \geq 20$ km and then stays more-or-less constant for larger values of D. We interpret this to mean that aerodynamic breakup does not affect the final crater shape of most $D \geq 20$ km craters.

For the second part, we used Magellan image headers and IDL software to calculate true diameters for the sinusoidally projected elongated craters found in the first part. This step was time-consuming enough that we were only able to remeasure 75 of the 185 craters described above. The measured 75 craters had D between 7.0 and 72.5 km. Of this set, we determined that only 23 were actually elliptical (about 30%). The maximum ellipticity of the 23 craters was 1.51.

The true diameter (TD) data can be used to scale results from our sinusoidally projected (SP) crater data: (185 SP elliptical craters/854 SP craters) $\times$ (23 TD craters/75 TD craters) $= 6.6\%$ elongated craters over all sizes, while (43 SP elliptical craters/303 SP craters) $\times$ (23 TD craters/75 TD craters) $= 4.4\%$ elongated craters for $D > 20$ km. The latter value is more appropriate for comparisons with the other terrestrial planet crater populations, and we find it a good match with the $\sim$5% elliptical crater fraction found on Mars and the Moon.

Note that many of our craters had irregularly shaped ejecta blankets, possibly, in some cases, similar to butterfly-shaped ejecta blankets on Mars. We hope to address this issue further in the future.

2.4. *Summary of Crater Surveys*

Mars, Venus, and the Moon all share roughly the same fraction of elliptical craters. This makes it unlikely that a unique population of low-angle impactors struck on Mars. It does suggest, however, that Mars's surface or atmospheric properties may, in some unknown way, be enhancing or protecting its population of butterfly-shaped ejecta blankets. We speculate that the process might be related to a mechanism which produces the lobed appearance of most of the ejecta blankets on Mars. Further study of this issue using laboratory impact experiments would be beneficial.

Since crater surveys themselves cannot explain the difference between the estimated elliptical crater populations and experimental predictions, we suggest that some other factor must be responsible. In the next section we will explore whether data from various laboratory impact experiments can explain the contradictory results.

3. A SIMPLE MODEL RELATING IMPACT AND CRATER GEOMETRIES

In this section, we use experimental data to generate a zeroth-order model describing the formation of elliptical craters. We use this procedure because existing documentation of the complex processes producing elliptical craters is mostly descriptive and does not readily lend itself to models. Accordingly, we simplify several real physical mechanisms while assuming that laboratory-derived relationships between crater ellipticity and projectile impact angle are reasonable when scaled to planetary craters. Our empirical model, however, is based on and is consistent with all of the presently available laboratory work on the topic.

Our procedure is described below. In Section 3.1, we discuss how impact angle, target strength, and crater ellipticity are qualitatively related. In Section 3.2, we develop a simple relationship between impact angle and crater ellipticity using the latest experimental data. In Section 3.3, we estimate the size of crater made by a projectile hitting Mars, and, finally, in Section 3.4, we bring together our estimates and describe our results.

3.1. *"Line Charges" and the Formation of Elliptical Craters*

The first part of our simple model makes use of a semiquantitative impact-explosion analogy (e.g., Melosh 1989) in which the projectile is treated as an explosive charge. An explosion digs a circular crater many times larger than the charge, which is often approximated as a point source.

To model the formation of an elongated crater, we envision the oblique impact as a linear explosive charge which excavates an elongated trench. The ellipticity ε of the trench is determined by the length of the line charge (L) in relation to the size of the final crater (D_c). In the limiting case where $L \ll D_c$, the line charge can be approximated as a point source producing a near-circular crater with $\varepsilon \to 1$. In the other extreme, where $L \approx D_c$, (imagine the crater made by a 1-km-long, 1-cm-wide stick of dynamite), $\varepsilon \to \infty$.

To clarify this issue, we use the following thought experiment. Suppose a 10-m "bomb" were capable of making a circular crater 100 m across. Reshaping the bomb into a line charge 10×20 m with the same explosive power as before might make a crater 100×110 m ($\varepsilon = 1.1$). Use of a stronger line charge would decrease the crater's ellipticity, since the charge would be more like a "point source" in relation to the crater size. If the 10-m bomb now made a 200-m crater, a 10×20-m line charge would make a crater 200×210 m ($\varepsilon = 1.05$). Conversely, a weaker line charge would increase the crater's ellipticity.

We extend this analogy to elongated impact craters by noting that in an oblique impact, the projectile's "footprint" on the target surface is an ellipse with an axis ratio of $1/\sin\theta$, where θ is the impact angle measured from horizontal. (This result follows readily from geometry.) The fact that the ratio of crater diameter over projectile diameter decreases with shallower impact angles has been noted elsewhere as well (Schultz and Gault 1990b, Schultz 1990). Thus, if factors like crater depth can be ignored, the footprint of the elongated projectile is roughly analogous to a linear explosive charge. (We caution, however, that this model does not accurately treat downrange sibling craters made by spalled projectile fragments). This rule of thumb, together with the idea that larger crater-to-projectile size ratios make elliptical crater formation more difficult, will be used in the next section to interpret experimental data.

3.2. *Experimental Data on Oblique Impacts*

The second part of our simple model draws upon measurements of experimental oblique impact craters drawn from the

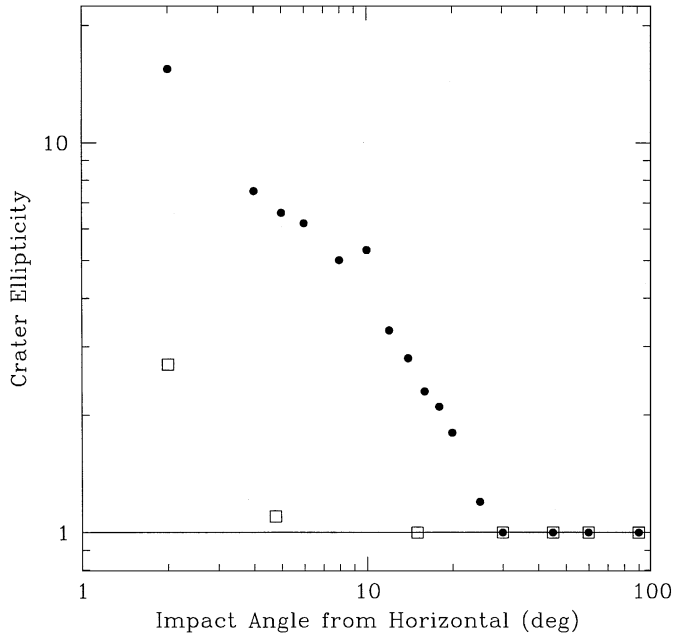

FIG. 7. Crater ellipticity vs impact angle, plotted for the laboratory impact experiments of GW78 (open squares) and C93 (solid circles). GW78 fired aluminum and pyrex spheres into sand targets at 6.4 km s^{-1}, while C93 fired aluminum spheres into aluminum targets at 6.5–7.0 km s^{-1}. A log–log plot is used to display power-law slopes.

literature. GW78 and C93 fired projectiles into sand (GW78) and aluminum (C93) targets at various angles. The results (crater ellipticity as a function of impact angle) are summarized in Fig. 7. As expected, craters are circular at steep impact angles and become increasingly elongated at shallow angles. Within uncertainty (which is large because GW78 only have two data points with $\varepsilon > 1.0$), the dependence of ellipticity on impact angle for elliptical craters follows the same $\sim\theta^{-1}$ power law in both studies. There is, however, a significant difference in the threshold angle for producing markedly elliptical craters: 4.75° for GW78 versus 25° for C93. This mismatch reveals that the threshold angle varies dramatically if the conditions of impact are changed and calls into question the assumption that centimeter-scale laboratory sand targets are an adequate analog for kilometer-scale planetary surfaces.

We now return to the impact–explosion analogy which, as noted above, suggests that crater ellipticity depends on the crater-to-projectile diameter ratio D_c/D_p. C93 report that, for vertical impacts of aluminum projectiles into aluminum targets at 6.5 to 7.0 km s^{-1}, the crater diameter is ~4.7 times the projectile diameter. Gault *et al.* (1974) show a ratio of ~61 for the vertical impact of an aluminum projectile onto sand at the 6.4 km s^{-1} speed used by GW78 for their threshold elliptical crater. Craters in sand are thus more than an order of magnitude larger than craters in aluminum caused by identical impactors, as expected given the difference in strength between the two target materials. If our line-charge model is correct, much shallower impact angles (corresponding to much more elongated projectile footprints) are needed to produce distorted craters in sand than in aluminum.

Next, we use the dependence of the elliptical crater threshold angle on the vertical impact crater-to-projectile diameter ratio to estimate the threshold angle θ_{ET} (elliptical threshold) for Mars. To do so, we first fit a power-law to the two available pairs of data for crater-to-projectile diameter ratio and threshold angle for elliptical crater production: (4.7, 25°) from C93 and (61, 4.75°) from Gault *et al.* (1974) and GW78. This technique is used with some trepidation, since planetary surfaces are most likely neither sand nor aluminum, but it must suffice in the absence of additional appropriate data or theoretical underpinning. The result is:

$$\theta_{Et} = 68.1^{\circ}\left(\frac{D_c}{D_p}\right)^{-0.648}. \quad (1)$$

Some caveats should be mentioned. The use of three-figure accuracy in Eq. (1) is not warranted, but these are the values we used for later calculations. We also caution that planetary topography will add additional uncertainty to this threshold value (Schultz 1990). This model also ignores material properties and absorbs variables like density contrast and velocity into the D_c/D_p ratio. Thus, Eq. (1) is certainly a simplification, but it matches all available observations.

3.3. Crater Sizes: Estimates from Scaling Laws

To get θ_{ET} from Eq. (1), we first must estimate D_c/D_p. Crater diameter (D_c), however, depends on many factors: projectile diameter, target strength, projectile and target densities, impact velocity, and target gravity (Melosh 1989). High-velocity laboratory shot experiments are often used to estimate D_c/D_p, since impact geometry as well as target and projectile properties can be controlled. Scaling laws derived from these experiments allow for interpretation of the crater records of planetary surfaces.

Currently, pi-group scaling laws yield the best fit relationship between laboratory impact experiments and hydrocode calculations (e.g., Holsapple and Schmidt 1982, summary in Melosh 1989). This technique combines the physically relevant parameters in an impact-crater event, such as transient crater diameter D_{at}, impact velocity V, target and projectile densities ρ_t and ρ_p, target strength Y, planetary gravity g, and projectile mass M into a number of dimensionless ratios which can be measured experimentally. The functional dependence of these values can then be determined by keeping all but the parameters of interest constant. Pi-group scaling has successfully been used to compare craters with similar dimensionless parameters, even though the impact events themselves had differing velocities, sizes, gravitational accelerations, and target strengths.

This procedure is simplified considerably if one assumes that the target and projectile densities are the same, the projectile is

spherical, and the craters are formed in the gravity regime. The transient crater diameter (before post-impact modifications take place) can then be estimated from

$$\pi_D = C_D \pi_2^{-\beta}, \tag{2}$$

with

$$\pi_D = D_{at}\left(\frac{\rho_t}{M}\right) \tag{3}$$

and

$$\pi_2 = \frac{1.61 g d_p}{V^2}. \tag{4}$$

Here, d_p is the diameter of the projectile, while C_D and β are experimentally determined constants, which, for a target of competent rock or saturated soil, are 1.6 and 0.22, respectively. By substituting into Eq. (2) and reorganizing, the transient crater diameter relation (D_{at}) is

$$D_{at} = \left(\frac{M}{\rho_t}\right)^{1/3}\left(\frac{1.61 g d_p}{V^2}\right)^{-\beta}. \tag{5}$$

This equation is appropriate for impactors striking perpendicular to the surface. Final rim-to-rim crater sizes are ~25% larger than the transient crater diameter (Melosh 1989), so our final crater size D_c is

$$D_c = 1.25\left(\frac{M}{\rho_t}\right)^{1/3}\left(\frac{1.61 g d_p}{V^2}\right)^{-\beta}. \tag{6}$$

3.4. Estimating Threshold Angles for Elliptical Crater Formation

Using Eq. (6), one can determine D_c/D_p for asteroids hitting competent rock (or saturated soil) on Venus, Mars, and the Moon. We estimate that a 1-km asteroid, with a density of 2500 kg m^{-3}, striking at a vertical impact velocity of 19, 12, and 13 km s^{-1}, respectively (the expected average impact velocity of asteroids crossing the orbit of Venus, Mars, and the Moon, as determined by Bottke *et al.* (1994)), should create a crater roughly 15, 15, and 19 km across, respectively. Inserting D_c/D_p into Eq. (1), we find that θ_{ET} for Venus, Mars, and the Moon is 12°, 12°, and 10°, respectively. Assuming the usual $\sin^2\theta$ probability distribution for random impact angles, we predict that between 3 and 5% of craters on these planets should be markedly elongated ($\varepsilon \geq 1.1$).

The above result compares favorably with the ~4–5% elliptical craters found in the various surveys described in this paper, but contrasts strongly with the 0.7% value derived solely from the GW78 data. Thus, our analysis suggests that there is no overabundance of elliptical craters on any of the terrestrial planets.

As a related aside, we mention that increasing the projectile size decreases the ratio D_c/D_p. For example, a 5-km asteroid striking Mars has a D_c/D_p ratio near 10. This change increases θ_{ET} to ~15°, enough to suggest that large impactors may have larger ellipticities. Though Fig. 5 suffers from small number statistics near 50 km, such large craters do appear to be more elongated than smaller ones.

4. A TEST OF THE SPIRALING MOONLET HYPOTHESIS

Finally, we address SL82's proposal that small moons orbiting in Mars's equatorial plane could have spiraled inward and struck at oblique angles, thereby causing an excess of elliptical craters. If true, Phobos and Deimos are the last survivors of a population of satellites which evolved inward by tidal drag until reaching the martian atmosphere. Support for this scenario comes from Phobos itself, which is tidally decaying rapidly enough that it will collide with Mars within the next 40 Myr (Burns 1992).

We tested the spiraling moonlet scenario as follows. Presumably, tidal forces over long time scales (~10^5–10^6 years) drag Phobos-like moonlets into Mars's atmosphere. At that point, aerodynamic drag becomes the dominant evolution mechanism, causing them to spiral inward quickly (hours to days, depending on the atmospheric density) until they hit the surface. Large moonlets, which are less susceptible to aerodynamic drag than small ones, should strike at shallower angles. Thus, a correlation between crater size and ellipticity should be evident in the resultant crater population, provided that Mars's atmospheric density was large enough to substantially modify the impact trajectories of the moonlets.

By numerically modeling the evolution of spiraling moonlets, we attempted to quantify this prediction. Our procedure consisted of three steps. First, we tracked the orbital evolution and impact trajectories of various sized moonlets in Mars's early atmosphere (Section 4.1). Next, we related the moonlet's impact angle to crater ellipticity using pi-group scaling theory and a model relating impact angle to crater shape (Section 4.2). Finally, we estimated the minor diameter of each crater (D_{min}) using experimental data so we could compare our model results to the survey results (Section 4.3).

4.1. Modeling the Orbital Decay and Impact of Spiraling Moonlets

4.1.1. Equations of motion for atmospheric entry. To track the orbital decay and impact trajectories of moonlets of various sizes entering Mars's early atmosphere, we integrated the equations of motion for atmosphere flight (e.g., Passey and Melosh 1980, Love and Brownlee 1991). We briefly review them here.

Upon entering an atmosphere, air molecules strike a projectile (assumed to be spherical), slowing it down and heating it while gravity reorients its trajectory toward the planetary surface. A bow shock forms in front of the projectile. The gas pressure there is

$$P \sim \rho_{\rm atm} v^2, \tag{7}$$

where $\rho_{\rm atm}$ is the density of the atmosphere and v is the velocity of the projectile (Melosh 1989). The pressure behind the projectile is negligible. The drag force on the projectile can be written as

$$\mathbf{F}_{\rm drag} = \mathbf{P}A = -C_{\rm drag}\rho_{\rm atm} A v^2 \hat{v}, \tag{8}$$

where A is the cross-sectional area of the projectile. The momentum change in a small time step dt is equal to the mass encountered times the relative velocity, plus a gravitational term,

$$d\mathbf{p} = \left(m\mathbf{g} - C_{\rm drag}\rho_{\rm atm} A v^2 \hat{v}\right), \tag{9}$$

where $C_{\rm drag}$ is a drag coefficient. Cited values for $C_{\rm drag}$ range from ~1.7 for a cylinder to 0.5 for a sphere (Hoerner 1965). We split the difference and choose $C_{\rm drag} = 1$ for our moonlets is limited by uncertainty in $C_{\rm drag}$. Expressing Eq. (9) in terms of v, we get

$$d\mathbf{v} = \left(\mathbf{g} - 0.75\frac{\rho_{\rm atm} v^2}{\rho_{\rm p} r}\hat{v}\right) dt, \tag{10}$$

where the spherical projectile's radius r and density $\rho_{\rm p}$ are now shown.

4.1.2. A simple early martian atmosphere. SL82 grouped their "elliptical-plus" craters in term of preservation state of the ejecta, which they took to be diagnostic of crater age. The "4" and "5" craters in their Appendix A, generally the craters with diameter >20 km, were considered to be the oldest. If this set of elliptical craters is more than 3.8 Gyr old, as is suggested by SL82, it is probable they were formed when Mars still had a thick, dense atmosphere (Owen 1992). To model this early atmosphere in our simulation, we assumed (i) it was primarily composed of CO_2, like the current atmosphere, and (ii) that the surface pressure and temperature were high enough to maintain liquid water on the surface (~1 bar and 273 K, respectively; Fanale *et al.* 1992). Using these values, we estimated that an early martian atmosphere would have had a scale height $H = 13.8$ km and a surface atmospheric density $\rho_{\rm atm} = 2.1$ kg m^{-3}. The density of the martian atmosphere at different altitudes is

$$\rho(z) = \rho_{\rm atm} e^{-(z/H)}, \tag{11}$$

where z is the height above sthe surface (Chamberlain and Hunten 1987). Equation (11) can be used in Eq. (10) to obtain the drag force on the projectile.

Table I
Results for "Spiraling Moonlet" Model

$D_{\rm moonlet}$ (km)	θ (°)	D_c[a] (km)	$\theta_{\rm ET}$[b] (°)	ε[c]	$D_{\rm min}$[d] (km)
0.2	10.4	2.46	14.2	1.6	1.83
0.5	6.9	5.03	16.1	2.8	2.65
1	5.2	8.64	17.7	4.1	3.58
2	4.0	14.8	19.5	5.8	4.95
5	2.8	30.3	22.1	9.5	7.44
10	2.2	52.0	24.3	13.2	10.4
20	1.7	89.3	26.8	18.9	(14.3)
50	1.2	183	30.4	30.4	(21.7)

[a] From Eq. (6). Crater diameters for vertical impact at 3.5 km s^{-1}, used for calculating $\theta_{\rm ET}$.
[b] From Eq. (1).
[c] From Eq. (12).
[d] From Eq. (13). The two values in parentheses correspond to crater diameters less than the projectile diameter, indicating that Eq. (13) is no longer a valid approximation.

4.1.3. Impact angles for spiraling moonlets. To track their orbital decay of each moonlet, we integrated Eq. (10) using a fourth-order Runge–Kutta numerical integrator (Press *et al.* 1989). The flight of the projectile in our code was two-dimensional to account for the curvature of Mars and its atmosphere. Each moonlet was given a density of 2500 kg m^{-3} and a size between 200 m and 50 km. We started them on circular orbits 100 km above the surface, presumably where atmospheric drag takes over from tidal drag, and followed them until they crossed Mars's surface, where impact angles were computed. We chose an integration time step of 10 s. Smaller time steps did not change the final results.

Our results show, as expected, an inverse correlation of impact angle (measured from the horizontal) with projectile size (Table I). This relationship is readily understood by considering the bodies' ballistic coefficients: larger moonlets (with a greater ratio of mass to cross-sectional area) are less deflected from their original paths by air drag than are smaller ones. Comparable relationships are expected for different model atmospheres and projectile properties.

4.2. Relating Impact Angle to Crater Ellipticity

We now find a relationship between impact angle (θ) and crater ellipticity (ε). The process is not straightforward. Each moonlet in Table I hit Mars with a different θ and impact velocity, complicating comparisons with (i) laboratory data, which used a nearly constant impact velocity near 6.5 km s^{-1}, and (ii) $\theta_{\rm ET}$, which uses D_c/D_p values calculated for vertical impacts. To begin the calculation, we found crater sizes for projectiles hitting Mars at a vertical impact velocity of 3.5 km s^{-1}, the approximate speed of an orbiting moonlet hitting Mars.

Using Eq. (6), we calculated crater sizes for each projectile size (Table I, third column). The ratio of the third and first columns yielded D_c/D_p, which we used with Eq. (1) to get θ_{ET} (Table I, fourth column). Crater ellipticity ε was then derived from the actual impact angle (θ) using relationships analogous to the ones illustrated in Fig. 7, but adjusted for the different θ_{ET} for typical Mars impacts. Recall that Fig. 7 shows that the GW78 and C93 data sets have power-law slopes near -1 when $\varepsilon > 1.0$. Expressing that relation in equation form, we got

$$\varepsilon = \max\left\{1.2\left(\frac{\theta_{Et}}{\theta}\right), 1.0\right\}. \tag{12}$$

The results of Eq. (12) for impacts on Mars are listed in the fifth column of Table I. The uncertainty in the numbers was estimated from Fig. 7 at ~20%.

4.3. Finding Crater Widths

To compare these ellipticity results with the survey data, we had to estimate the minor diameter of each crater (D_{min}). Thus, a relationship between impact angle and crater geometry was needed. The best available data set for doing so is that of C93; we use it despite the possibility that such experimental data may not be applicable for kilometer-scale craters on Mars. We minimized the effects of size and materials, however, by examining only relative geometrical parameters and avoiding direct reference to the kinetic and material properties of the projectile and target.

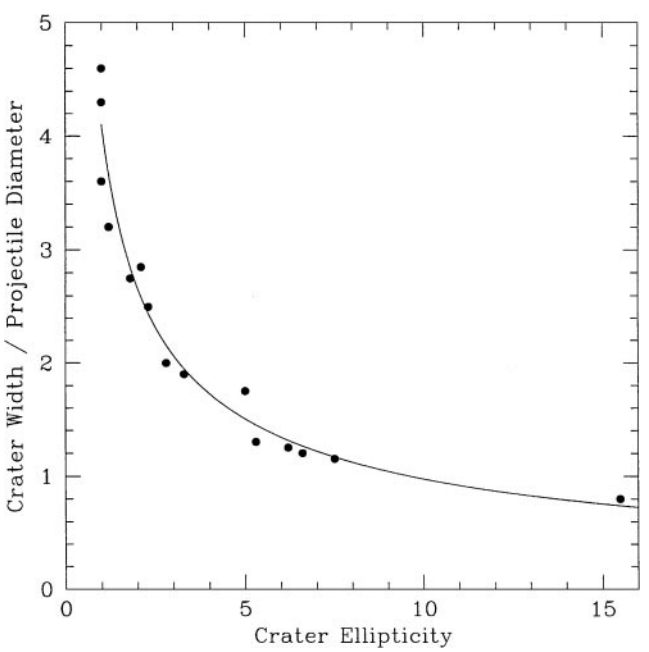

FIG. 8. The minimum diameter, or width, of each crater from C93 is scaled by the projectile's diameter and plotted against the crater's ellipticity ε. The solid curve was found using a least squares fit method. It has the functional form $y = 4.11x^{-0.625}$.

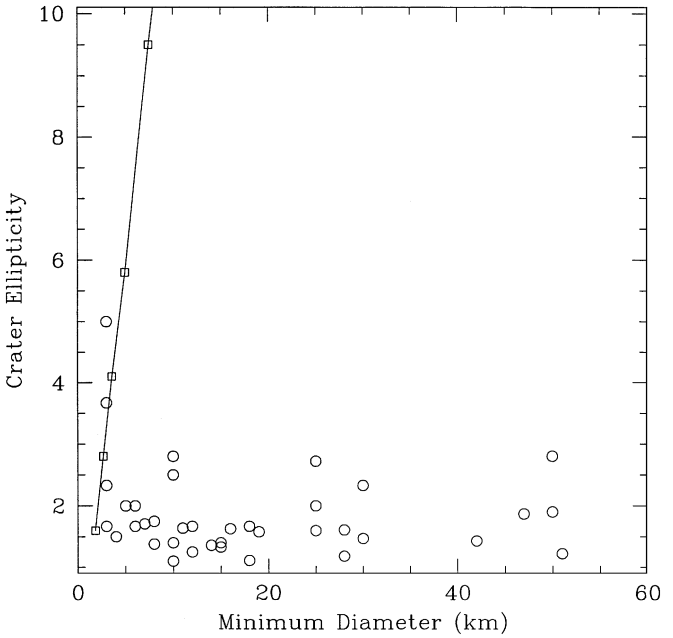

FIG. 9. The results from the martian "spiraling moonlet" orbital decay hypothesis (Table I, open squares) are plotted against the 43 oldest Likely and Possible craters from Schultz and Lutz-Garihan (1982) (i.e., their "4" and "5" craters). The mismatch between the model results and the data is apparent, suggesting that few elliptical craters on Mars were produced by this mechanism.

Figure 7 shows that ellipticity increases with decreasing impact angle. So, by taking the C93 crater widths, scaling them by the projectile diameter, and plotting them against ellipticity, we found that major diameter grows and minor diameter shrinks with decreasing impact angle, if all else is equal (Fig. 8). Using a least squares fit, the C93 data exhibited the following geometrical relationship:

$$D_{min} = C\varepsilon^{-0.625}, \tag{13}$$

where C is a constant (4.11 for the C93 data) and all other parameters are held constant. Note that this relationship does not include the effect of local and regional slopes which can affect the impact angle. Since the global average regional slope on all surfaces is zero, however, we expect that slope effect would only introduce some additional scatter to the plotted points.

Equation (13) matches the C93 data within 5% if C is set equal to the diameter of the crater resulting from a vertical impact at the same speed (Table I, third column). By applying this equation to martian craters, we are assuming that the geometrical interrelationships of all elliptical craters are the same, even though different impact angles make craters of the same ellipticity when particular circumstances are applied. Using the

appropriate values from Table I, we use Eq. (13) to yield D_{min} (Table I, sixth column). The last two values of that column (corresponding to ellipticity values much larger than the maximum observed) are smaller than the projectile diameter and are probably not meaningful. We estimate a ~50% upper limit of the uncertainty in each column.

The points defined by the leftmost two columns of Table I are plotted in Fig. 9 along with the 43 oldest Likely and Possible craters ("4" and "5" craters from SL82's Appendix A). Note that this plot also includes craters with minimum diameters $\leq$5 km that were Omitted in Appendix A. Figure 9 shows that outcomes of the spiraling moonlet scenario does not match observations.

Using this model with Mars's current low-density atmosphere is also revealing. Our model suggests that large and small moonlets alike should strike Mars at impact angles less than 1° from the horizontal. Based on the results from Table I, this should create a population of extraordinarily elliptical craters. Such a population is not observed. Thus, while we do not rule out the possibility that a few singular events such as this have occurred, we believe that spiraling moonlets did not produce a significant fraction of elliptical craters on Mars.

5. CONCLUSIONS

Our study found that despite differences between cataloged elliptical craters lists, the total number of elongated craters represent approximately 5% of the martian crater population, which is reasonably close to the abundance measurements of previous studies. This fraction matches comparable values obtained for the Moon and Venus.

Interpolating between impact experiment data produced in sand and aluminum, we derived new elliptical crater threshold angles for Venus, Mars, and the Moon. Our results suggest that $\theta_{ET} \leq 12°$ rather than $\leq 4.75°$ (GW78) provides a better match to observations within uncertainty given a randomly flying projectile population. Our new value for θ_{ET} yields an expected elongated crater abundance of 4%, which is close to the observed value.

Tests of the spiraling moonlet hypothesis, an alternative way to make elliptical craters, show a strong correlation between minimum size and ellipticity which is not seen in the oldest crater data. Thus, we believe that this additional mechanism is unnecessary, though we do not rule out the possibility that a small fraction of the martian elliptical crater population was made this way.

APPENDIX A

For reference, we include our martian elliptical crater survey data derived from SL82 and B88. These craters were designated Likely, Possible, and Unlikely according to the criteria described in Section 2.1. The table also includes each crater's index number (according to the SL82 or B88 surveys), latitude, longitude, minimum and maximum diameter, and ellipticity ε. "B" stands for B88, while "S" stands for SL82.

Martian Elliptical Crater Data

#	REF	Lat. (°)	Lon. (°)	D_{max} (km)	D_{min} (km)	ε	Quality
30	S	41.50	236.00	40.0	30.0	1.33	Likely
2	S	41.00	137.50	10.0	9.0	1.11	Likely
3	B	40.78	137.34	12.2	6.7	1.82	Likely
12	S	38.50	50.50	20.0	18.0	1.11	Likely
27	S	38.50	256.00	10.0	8.0	1.25	Likely
20	S	37.50	317.00	9.0	7.0	1.29	Likely
5	S	36.00	95.00	9.0	5.0	1.80	Likely
10	S	36.00	56.50	10.0	7.0	1.43	Likely
15	B	34.17	330.57	23.7	18.3	1.30	Likely
4	B	33.84	140.10	23.5	11.3	2.08	Likely
23	B	32.65	211.29	48.0	25.2	1.90	Likely
31	S	31.50	219.50	17.0	11.0	1.55	Likely
22	B	31.41	219.67	15.8	10.6	1.49	Likely
32	S	28.50	174.50	8.0	7.0	1.14	Likely
43	B	26.51	9.96	53.2	26.3	2.02	Likely
35	S	26.50	115.50	10.0	8.0	1.25	Likely
42	B	26.06	15.19	31.1	16.2	1.92	Likely
52	S	26.00	15.00	30.0	18.0	1.67	Likely
28	B	25.19	97.45	33.4	19.9	1.68	Likely
37	S	25.00	97.50	35.0	18.0	1.94	Likely
62	B	24.09	296.22	13.0	7.8	1.67	Likely
68	B	23.91	271.14	11.7	6.3	1.86	Likely
41	B	19.02	5.86	42.5	25.2	1.69	Likely
58	S	19.00	315.50	44.0	30.0	1.47	Likely
55	B	18.74	315.77	42.2	27.1	1.56	Likely
40	B	18.41	36.30	9.8	6.2	1.58	Likely
31	B	16.53	53.35	29.1	18.7	1.56	Likely
43	S	16.50	60.00	30.0	25.0	1.20	Likely
53	B	16.24	357.00	137.7	42.9	3.21	Likely
59	S	16.00	357.00	140.0	50.0	2.80	Likely
86	S	16.00	258.00	30.0	19.0	1.58	Likely
78	S	15.50	283.50	26.0	16.0	1.63	Likely
87	S	15.00	229.00	9.0	7.0	1.29	Likely
88	B	13.83	192.98	13.4	6.6	2.03	Likely
81	S	13.50	296.50	11.0	8.0	1.38	Likely
34	S	13.00	169.50	12.0	9.0	1.33	Likely
36	B	12.46	49.83	15.9	8.5	1.87	Likely
83	B	11.08	241.81	10.6	6.2	1.71	Likely
46	S	9.00	80.50	15.0	12.0	1.25	Likely
89	S	8.50	264.00	10.0	6.0	1.67	Likely
77	B	7.89	262.23	14.0	8.3	1.69	Likely
73	S	7.50	333.00	14.0	11.0	1.27	Likely
88	S	6.50	256.00	11.0	10.0	1.10	Likely
93	S	5.50	224.00	10.0	8.0	1.25	Likely
35	B	5.46	57.53	9.2	6.4	1.44	Likely
72	S	5.00	316.00	19.0	11.0	1.73	Likely
80	S	5.00	312.00	20.0	18.0	1.11	Likely
80	B	4.82	235.16	26.8	20.1	1.33	Likely
71	S	3.50	320.00	10.0	8.0	1.25	Likely
25	B	2.81	172.77	18.3	11.5	1.59	Likely
26	B	2.25	172.64	28.9	23.7	1.22	Likely
60	B	2.02	344.90	13.0	9.1	1.43	Likely

APPENDIX A—*Continued*

#	REF	Lat. (°)	Lon. (°)	D_{max} (km)	D_{min} (km)	ε	Quality
68	S	2.00	345.00	15.0	12.0	1.25	Likely
47	B	.74	22.86	18.8	11.9	1.58	Likely
56	S	.50	23.00	20.0	15.0	1.33	Likely
113	S	−1.00	29.50	12.0	10.0	1.20	Likely
115	S	−1.50	355.00	10.0	9.0	1.11	Likely
111	S	−2.00	40.50	22.0	20.0	1.10	Likely
115	B	−4.97	3.42	21.3	13.7	1.55	Likely
96	S	−5.50	169.00	10.0	6.0	1.67	Likely
132	B	−6.97	324.87	27.9	23.6	1.18	Likely
130	S	−7.50	272.00	18.0	11.0	1.64	Likely
133	B	−8.15	337.29	40.3	26.4	1.53	Likely
91	B	−9.21	160.11	14.6	7.1	2.06	Likely
116	B	−9.85	11.09	36.8	25.4	1.45	Likely
98	S	−10.00	148.50	16.0	10.0	1.60	Likely
131	S	−11.50	282.00	9.0	7.0	1.29	Likely
120	S	−13.50	343.50	24.0	16.0	1.50	Likely
128	B	−13.96	343.54	22.9	14.6	1.57	Likely
116	S	−14.50	338.50	12.0	10.0	1.20	Likely
118	S	−14.50	329.00	15.0	13.0	1.15	Likely
106	B	−14.75	82.73	21.2	12.6	1.68	Likely
102	S	−15.00	83.00	23.0	12.0	1.92	Likely
125	B	−16.71	7.11	15.2	11.0	1.38	Likely
98	B	−16.85	151.05	18.7	9.4	1.99	Likely
149	B	−17.45	225.34	16.4	11.1	1.48	Likely
107	S	−18.00	72.00	18.0	15.0	1.20	Likely
125	S	−18.00	348.50	10.0	6.0	1.67	Likely
136	S	−18.00	302.00	15.0	13.0	1.15	Likely
122	S	−18.50	348.00	33.0	28.0	1.18	Likely
133	S	−19.00	306.00	50.0	25.0	2.00	Likely
123	S	−19.50	340.50	14.0	11.0	1.27	Likely
109	S	−21.50	73.00	15.0	11.0	1.36	Likely
96	B	−21.73	178.11	15.5	11.9	1.30	Likely
108	S	−23.50	71.50	21.0	15.0	1.40	Likely
103	B	−23.99	144.77	16.8	8.4	2.00	Likely
127	S	−24.50	319.00	16.0	10.0	1.60	Likely
114	S	−25.00	9.50	88.0	47.0	1.87	Likely
121	B	−25.04	10.72	81.8	46.1	1.77	Likely
140	S	−27.00	249.00	9.0	7.0	1.29	Likely
122	B	−27.86	5.74	20.7	13.9	1.49	Likely
105	B	−28.94	103.24	19.8	13.8	1.43	Likely
110	S	−30.00	52.50	20.0	18.0	1.11	Likely
156	B	−30.99	158.99	21.4	14.7	1.46	Likely
154	S	−31.00	159.00	19.0	14.0	1.36	Likely
160	S	−31.00	4.00	9.0	8.0	1.13	Likely
199	B	−31.65	232.93	17.3	11.3	1.53	Likely
178	B	−33.16	55.65	11.1	6.6	1.68	Likely
151	S	−34.50	174.50	62.0	51.0	1.22	Likely
168	S	−35.50	241.50	24.0	10.0	2.40	Likely
200	B	−35.63	241.25	24.8	10.0	2.48	Likely
201	B	−41.02	219.91	19.6	8.9	2.20	Likely
14	B	45.56	344.28	9.2	5.0	1.84	Possible

APPENDIX A—*Continued*

#	REF	Lat. (°)	Lon. (°)	D_{max} (km)	D_{min} (km)	ε	Quality
17	S	45.50	344.50	12.0	6.0	2.00	Possible
25	S	45.50	259.50	9.0	8.0	1.13	Possible
14	S	45.00	30.00	10.0	8.0	1.25	Possible
20	B	44.97	292.97	10.8	7.6	1.42	Possible
17	B	44.28	326.40	8.7	5.7	1.53	Possible
7	B	42.89	64.52	8.3	5.5	1.51	Possible
11	S	40.00	53.50	12.0	10.0	1.20	Possible
9	B	38.33	1.34	20.5	14.6	1.40	Possible
19	S	38.00	338.50	7.0	6.0	1.17	Possible
21	B	37.78	289.32	33.6	25.5	1.32	Possible
28	S	37.50	268.50	9.0	8.0	1.13	Possible
19	B	33.85	311.32	52.0	37.1	1.40	Possible
13	B	31.67	341.39	27.1	17.7	1.53	Possible
4	S	31.00	96.50	10.0	9.0	1.11	Possible
29	B	28.97	82.03	28.9	8.8	3.28	Possible
85	S	27.00	262.50	12.0	8.0	1.50	Possible
90	S	27.00	212.00	15.0	13.0	1.15	Possible
38	S	26.50	91.50	10.0	8.0	1.25	Possible
42	S	26.50	68.50	34.0	15.0	2.27	Possible
53	S	26.50	10.00	68.0	25.0	2.72	Possible
86	B	25.53	186.55	12.4	9.4	1.32	Possible
74	B	25.48	269.74	22.7	11.2	2.03	Possible
51	S	25.00	35.50	9.0	8.0	1.13	Possible
76	S	25.00	275.00	10.0	9.0	1.11	Possible
92	S	25.00	182.00	20.0	18.0	1.11	Possible
75	S	24.00	296.00	14.0	8.0	1.75	Possible
63	B	23.29	285.24	36.9	27.2	1.36	Possible
32	B	22.66	55.36	20.6	16.4	1.26	Possible
64	B	22.14	281.83	29.2	20.9	1.40	Possible
41	S	22.00	79.00	9.0	5.0	1.80	Possible
62	S	22.00	353.00	12.0	10.0	1.20	Possible
66	S	22.00	335.00	12.0	7.0	1.71	Possible
74	S	21.00	309.00	10.0	5.0	2.00	Possible
61	S	20.50	355.50	15.0	13.0	1.15	Possible
76	B	18.63	240.09	25.5	13.6	1.88	Possible
37	B	16.98	23.43	10.7	7.0	1.53	Possible
66	B	15.55	283.43	25.3	14.7	1.72	Possible
60	S	15.50	357.50	14.0	10.0	1.40	Possible
51	B	14.55	3.90	29.6	16.7	1.77	Possible
47	S	14.00	71.00	8.0	5.0	1.60	Possible
59	B	13.86	352.51	42.6	14.6	2.92	Possible
33	B	13.83	70.85	7.8	5.6	1.39	Possible
48	S	13.50	72.00	10.0	9.0	1.11	Possible
49	S	13.00	70.50	11.0	9.0	1.22	Possible
61	B	11.84	330.23	31.7	20.4	1.55	Possible
67	S	11.00	341.50	10.0	8.0	1.25	Possible
82	S	11.00	292.50	14.0	11.0	1.27	Possible
79	B	10.22	241.42	10.5	5.5	1.91	Possible
84	S	9.50	292.50	9.0	8.0	1.13	Possible
50	B	7.83	20.93	37.6	28.4	1.32	Possible
70	S	6.00	320.00	11.0	9.0	1.22	Possible
78	B	4.83	255.33	30.3	22.7	1.33	Possible
34	B	4.55	57.94	23.2	12.1	1.92	Possible

APPENDIX A—*Continued*

#	REF	Lat. (°)	Lon. (°)	D_{max} (km)	D_{min} (km)	ε	Quality
57	S	4.00	11.00	20.0	12.0	1.67	Possible
49	B	2.85	32.75	11.5	7.1	1.62	Possible
48	B	2.77	30.11	40.4	30.5	1.32	Possible
83	S	2.00	277.00	7.0	6.0	1.17	Possible
71	B	.97	312.44	13.2	6.4	2.06	Possible
94	S	.50	204.50	11.0	10.0	1.10	Possible
146	S	−.50	202.00	11.0	10.0	1.10	Possible
146	B	−.88	269.28	15.4	10.2	1.51	Possible
145	B	−1.52	250.91	10.6	6.9	1.54	Possible
112	S	−2.00	24.00	13.0	10.0	1.30	Possible
147	B	−6.23	227.86	13.2	9.6	1.38	Possible
104	S	−8.00	63.00	10.0	5.0	2.00	Possible
113	B	−8.61	23.26	19.3	14.2	1.36	Possible
138	B	−9.05	288.47	16.6	12.5	1.33	Possible
139	S	−11.50	243.50	11.0	9.0	1.22	Possible
107	B	−11.95	47.90	17.3	12.7	1.36	Possible
97	S	−12.00	173.50	60.0	42.0	1.43	Possible
105	S	−12.50	59.00	10.0	9.0	1.11	Possible
117	S	−12.50	331.50	21.0	15.0	1.40	Possible
114	B	−12.67	16.09	13.0	9.1	1.43	Possible
119	S	−14.00	336.00	45.0	28.0	1.61	Possible
131	B	−14.09	336.25	42.6	28.2	1.51	Possible
106	S	−16.50	81.00	17.0	14.0	1.21	Possible
148	B	−17.54	264.32	81.6	18.3	4.46	Possible
142	B	−18.18	248.83	7.8	5.1	1.53	Possible
97	B	−18.87	155.97	10.4	7.0	1.49	Possible
142	S	−19.00	266.00	12.0	10.0	1.20	Possible
150	S	−19.00	182.50	15.0	10.0	1.50	Possible
124	S	−20.00	339.50	16.0	12.0	1.33	Possible
137	B	−20.42	315.65	10.6	7.9	1.34	Possible
141	B	−20.95	287.84	96.9	46.3	2.09	Possible
134	S	−21.00	305.00	70.0	30.0	2.33	Possible
137	S	−21.00	287.50	95.0	50.0	1.90	Possible
141	S	−22.00	259.50	20.0	16.0	1.25	Possible
104	B	−22.24	111.47	14.2	10.7	1.33	Possible
123	B	−24.00	18.97	12.4	8.1	1.53	Possible
143	S	−24.00	244.50	8.0	5.0	1.60	Possible
99	B	−24.32	149.40	11.0	8.0	1.38	Possible
102	B	−25.35	144.62	15.3	10.0	1.53	Possible
101	B	−25.37	144.23	34.1	12.4	2.75	Possible
135	B	−26.07	357.50	11.8	7.4	1.59	Possible
155	B	−26.09	204.79	44.8	22.0	2.04	Possible
100	S	−26.50	161.50	40.0	25.0	1.60	Possible
149	S	−26.50	210.50	10.0	9.0	1.11	Possible
100	B	−26.55	143.52	13.7	8.6	1.59	Possible
95	B	−27.09	163.00	38.7	29.9	1.29	Possible
153	B	−27.48	212.86	28.8	21.0	1.37	Possible
143	B	−27.96	284.69	37.3	14.2	2.63	Possible
144	B	−28.32	280.03	13.8	9.8	1.41	Possible
192	B	−30.27	288.42	10.3	7.0	1.47	Possible
181	B	−31.33	39.52	7.4	5.7	1.30	Possible
182	B	−31.79	40.09	23.3	16.9	1.38	Possible
158	S	−34.00	82.00	11.0	8.0	1.38	Possible
189	B	−34.53	326.41	63.9	37.4	1.71	Possible

APPENDIX A—*Continued*

#	REF	Lat. (°)	Lon. (°)	D_{max} (km)	D_{min} (km)	ε	Quality
170	B	−36.84	74.01	16.3	8.9	1.83	Possible
159	S	−37.00	74.00	25.0	10.0	2.50	Possible
168	B	−37.61	91.12	30.5	13.8	2.21	Possible
177	B	−37.61	50.66	15.5	10.1	1.53	Possible
161	B	−37.63	117.04	12.1	8.6	1.41	Possible
158	B	−38.25	173.77	28.4	15.6	1.82	Possible
162	S	−39.00	327.50	10.0	6.0	1.67	Possible
190	B	−39.85	321.35	22.7	16.7	1.36	Possible
185	B	−40.89	37.45	11.2	7.0	1.60	Possible
170	S	−41.00	220.00	28.0	10.0	2.80	Possible
159	B	−46.12	119.32	29.1	19.1	1.52	Possible
191	B	−46.61	284.24	15.6	11.2	1.39	Possible
157	B	−46.80	174.67	22.0	17.3	1.27	Possible
5	B	44.15	67.46	17.1	12.1	1.41	Unlikely
24	S	41.50	268.50	5.0	5.0	1.00	Unlikely
23	S	39.50	282.50	2.0	2.0	1.00	Unlikely
29	S	33.50	233.00	22.0	17.0	1.29	Unlikely
77	S	30.00	273.00	42.0	32.0	1.31	Unlikely
40	S	29.00	82.00	30.0	10.0	3.00	Unlikely
39	S	26.50	91.50	10.0	10.0	1.00	Unlikely
50	S	26.00	27.00	10.0	10.0	1.00	Unlikely
33	S	25.00	142.00	29.0	28.0	1.04	Unlikely
54	S	24.50	3.00	10.0	9.0	1.11	Unlikely
30	B	24.49	70.25	14.5	4.4	3.30	Unlikely
44	S	18.00	64.00	8.0	8.0	1.00	Unlikely
65	S	17.00	341.50	15.0	12.0	1.25	Unlikely
27	B	13.21	168.67	43.5	32.4	1.34	Unlikely
45	S	9.00	88.00	9.0	9.0	1.00	Unlikely
72	B	5.86	292.79	5.1	1.7	3.00	Unlikely
52	B	3.91	10.66	18.7	12.8	1.46	Unlikely
112	B	−2.73	24.55	15.9	8.9	1.79	Unlikely
129	B	−2.85	358.90	19.6	15.2	1.29	Unlikely
128	S	−4.00	312.00	12.0	11.0	1.09	Unlikely
103	S	−11.00	76.50	18.0	10.0	1.80	Unlikely
121	S	−15.00	345.00	20.0	19.0	1.05	Unlikely
144	S	−15.50	238.00	19.0	18.0	1.06	Unlikely
134	B	−19.91	339.40	15.1	11.6	1.30	Unlikely
163	S	−31.00	272.50	20.0	15.0	1.33	Unlikely
156	S	−33.00	82.00	13.0	5.0	2.60	Unlikely
152	S	−35.00	165.50	32.0	30.0	1.07	Unlikely
153	S	−35.50	167.00	20.0	20.0	1.00	Unlikely
15	S	34.50	8.50	6.0	4.0	1.50	Omit-Likely
75	B	29.20	256.28	9.8	4.2	2.33	Omit-Likely
69	B	27.07	273.78	7.7	4.4	1.75	Omit-Likely
84	B	22.42	204.45	6.5	4.0	1.63	Omit-Likely
126	B	−11.02	359.61	7.9	4.5	1.76	Omit-Likely
136	B	−24.05	319.73	6.5	3.5	1.86	Omit-Likely
151	B	−26.71	221.62	6.9	4.0	1.73	Omit-Likely
101	S	−27.00	123.00	11.0	3.0	3.67	Omit-Likely
161	S	−32.50	359.50	6.0	4.0	1.50	Omit-Likely
183	B	−33.62	29.19	7.0	1.7	4.12	Omit-Likely
22	S	45.50	291.00	4.0	2.0	2.00	Omit-Possible
13	S	44.00	63.50	5.0	3.0	1.67	Omit-Possible
7	S	41.50	80.00	15.0	3.0	5.00	Omit-Possible

APPENDIX A—*Continued*

#	REF	Lat. (°)	Lon. (°)	D_{max} (km)	D_{min} (km)	ϵ	Quality
16	B	37.62	336.97	7.3	4.4	1.66	Omit-Possible
26	S	35.00	261.50	7.0	3.0	2.33	Omit-Possible
36	S	26.50	114.00	8.0	4.0	2.00	Omit-Possible
67	B	23.23	275.77	7.8	4.8	1.63	Omit-Possible
64	S	21.00	354.50	7.0	3.0	2.33	Omit-Possible
46	B	2.03	38.32	5.8	3.3	1.76	Omit-Possible
110	B	−3.73	44.06	8.5	4.5	1.89	Omit-Possible
90	B	−13.18	159.94	7.0	3.7	1.89	Omit-Possible

ACKNOWLEDGMENTS

We thank N. Barlow for providing her elliptical crater data set and H. J. Melosh and J. Burns for useful commentary and discussions. We also appreciate the work of N. Barlow and an anonymous reviewer for constructive and thoughtful critiques of the manuscript. For use of the Mars Multi-Scale Map, we thank C. J. Hamilton of Los Alamos National Laboratory. For use of the Venus crater data, we thank G. G. Schaber (U.S. Geological Survey) and R. Herrick (LPI). This project was supported by D. Tytell's Flintridge Foundation summer undergraduate research fellowship (SURF) at Caltech, T. Glotch's NASA/New York Spacegrant summer undergraduate research internship, S. G. Love's O. K. Earl Prize Fellowship at Caltech, and W. F. Bottke's Texaco Prize Fellowship at Caltech. Additional support was provided by NASA Grant NAGW-310. The research described in this paper was partially performed by the Jet Propulsion Laboratory, California Institute of Technology, under a contract with NASA.

REFERENCES

Barlow, N. G. 1988. Crater size-frequency distributions and a revised martian relative chronology. *Icarus* **75**, 285–305.

Bottke, W. F., and H. J. Melosh 1996a. The formation of asteroid satellites and doublet craters by planetary tidal forces. *Nature* **381**, 51–53.

Bottke, W. F., and H. J. Melosh 1996b. The formation of binary asteroids and doublet craters. *Icarus* **124**, 372–391.

Bottke, W. F., M. C. Nolan, R. Greenberg, and R. A. Kolvoord 1994. Collisional lifetimes and impact statistics of near-Earth asteroids. In *Hazards Due to Comets and Asteroids* (T. Gehrels and M. S. Matthews, Eds.), pp. 337–357. Univ. of Arizona Press, Tucson.

Burchell, M. J., and N. G. Mackay 1998. Crater ellipticity in hypervelocity impacts on metals. *J. Geophys. Res.* **103**, 22,761–22,774.

Burns, J. A. 1992. Contradictory clues as to the origin of the martian moons. In *Mars* (H. H. Kieffer, B. M. Jakosky, C. W. Snyder, and M. S. Matthews, Eds.), pp. 1257–1282. Univ. of Arizona Press, Tucson.

Chamberlain, J. W., and D. M. Hunten 1987. *Theory of Planetary Atmospheres. An Introduction to Their Physics and Chemistry.* Academic Press, Orlando, FL.

Christiansen, E. L., E. D. Cytowski, and J. Ortega 1993. Highly oblique impacts into thick and thin targets. *Int. J. Impact Eng.* **14**, 157–168.

Fanale, F. P., S. E. Postawko, J. B. Pollack, M. H. Carr, and R. O. Pepin 1992. Mars: Epochal climate change and volatile history. In *Mars* (H. H. Kieffer, B. M. Jakosky, C. W. Snyder, and M. S. Matthews, Eds.), pp. 1135–1179. Univ. of Arizona Press, Tucson.

Gault D. E., and J. A. Wedekind 1978. Experimental studies of oblique impacts. *Proc. Lunar. Planet. Sci. Conf.* **9**, 3843–3875.

Gault D. E., F. Hörz, D. E. Brownlee, and J. B. Hartung 1974. Mixing of the lunar regolith. *Proc. Lunar. Planet. Sci. Conf.* **5**, 2365–2386.

Hoerner, S. F. 1965. *Fluid-Dynamic Drag.* Hoerner, Midland Park, NJ.

Holsapple, K. A., and R. M. Schmidt 1982. On the scaling of crater dimensions 2. Impact processes. *J. Geophys. Res.* **87**, 1849–1870.

Love, S. G., and D. E. Brownlee 1991. Heating and thermal transformation of micrometeoroids entering the Earth's atmosphere. *Icarus* **89**, 26–46.

Melosh, H. J. 1989. *Impact Cratering: A Geologic Process.* Oxford Univ. Press, New York.

Owen, T. 1992. The composition and early history of the atmosphere of Mars. In *Mars* (H. H. Kieffer, B. M. Jakosky, C. W. Snyder, and M. S. Matthews, Eds.), pp. 818–834. Univ. of Arizona Press, Tucson.

Passey, Q., and H. J. Melosh 1980. The effects of atmospheric break-up on crater field formation. *Icarus* **42**, 211–233.

Press, W. H., B. P. Flannery, S. A. Teukolsky, and W. T. Vetterling 1989. *Numerical Recipes: The Art of Scientific Computing.* Cambridge Univ. Press, Cambridge.

Schaber, G. G., R. L. Kirk, and R. G. Strom 1998. *Data Base of Impact Craters on Venus Based on Analysis of Magellan Radar Images and Altimetry Data*, USGS Open-File Report 98–104, http://wwwflag.wr.usgs.gov/USGSFlag/Space/venus/.

Schultz, P. H. 1990. Evidence for atmospheric effects on martian crater shape. *Lunar Planet. Sci* **21**, 1097.

Schultz, P. H., and D. E. Gault 1990a. Decapitated impactors in the laboratory and on the planets. *Lunar Planet. Sci.* **21**, 1099.

Schultz, P. H., and D. E. Gault 1990b. Prolonged global catastrophies from oblique impacts. *Geol. Soc. Am. Spec. Pap.* **247**, 239–261.

Schultz, P. H., and A. B. Lutz-Garihan 1982. Grazing impacts on Mars: A record of lost satellites. *J. Geophys. Res.* **87**, A84–A96.

Shoemaker, E. M. 1962. Interpretation of lunar craters. In *Physics and Astronomy of the Moon* (Z. Kopal, Ed.), pp. 283–359. Academic Press, New York.